Title: The geomorphology, color, and thermal properties of Ryugu: Implications for parent-body processes

Short title: Hayabusa2 globally imaged asteroid Ryugu.

Authors: S. Sugita[1,2*], R. Honda[3], T. Morota[4], S. Kameda[5], H. Sawada[6], E. Tatsumi[1], M. Yamada[2], C. Honda[7], Y. Yokota[6,3], T. Kouyama[8], N. Sakatani[6], K. Ogawa[9], H. Suzuki[10], T. Okada[6,1], N. Namiki[11,12], S. Tanaka[6,12], Y. Iijima[6§], K. Yoshioka[1], M. Hayakawa[6], Y. Cho[1], M. Matsuoka[6], N. Hirata[7], N. Hirata[9], H. Miyamoto[1], D. Domingue[13], M. Hirabayashi[14], T. Nakamura[15], T. Hiroi[16], T. Michikami[17], P. Michel[18], R. -L. Ballouz[6,19], O. S. Barnouin[20], C. M. Ernst[20], S. E. Schröder[21], H. Kikuchi[1], R. Hemmi[1], G. Komatsu[22,2], T. Fukuhara[5], M. Taguchi[5], T. Arai[23], H. Senshu[2], H. Demura[7], Y. Ogawa[7], Y. Shimaki[6], T. Sekiguchi[24], T. G. Müller[25], A. Hagermann[26], T. Mizuno[6], H. Noda[11], K. Matsumoto[11,12], R. Yamada[7], Y. Ishihara[6†], H. Ikeda[27], H. Araki[11], K. Yamamoto[11], S. Abe[28], F. Yoshida[2], A. Higuchi[11], S. Sasaki[29], S. Oshigami[11], S. Tsuruta[11], K. Asari[11], S. Tazawa[11], M. Shizugami[11], J. Kimura[29], T. Otsubo[30], H. Yabuta[31], S. Hasegawa[6], M. Ishiguro[32], S. Tachibana[1], E. Palmer[13], R. Gaskell[13], L. Le Corre[13], R. Jaumann[21], K. Otto[21], N. Schmitz[21], P. A. Abell[33], M. A. Barucci[34], M. E. Zolensky[33], F. Vilas[13], F. Thuillet[18], C. Sugimoto[1], N. Takaki[1], Y. Suzuki[1], H. Kamiyoshihara[1], M. Okada[1], K. Nagata[8], M. Fujimoto[6], M. Yoshikawa[6,12], Y. Yamamoto[6,12], K. Shirai[6], R. Noguchi[6], N. Ogawa[6], F. Terui[6], S. Kikuchi[6], T. Yamaguchi[6‡], Y. Oki[1], Y. Takao[1], H. Takeuchi[6], G. Ono[27], Y. Mimasu[6], K. Yoshikawa[27], T. Takahashi[6], Y. Takei[6,27], A. Fujii[6], C. Hirose[27], S. Nakazawa[6], S. Hosoda[6], O. Mori[6], T. Shimada[6], S. Soldini[6], T. Iwata[6,12], M. Abe[6,12], H. Yano[6,12], R. Tsukizaki[6], M. Ozaki[6,12], K. Nishiyama[6], T. Saiki[6], S. Watanabe[4,6], Y. Tsuda[6,12].

Affiliations:

1. The University of Tokyo, Tokyo 113-0033, Japan.
2. Planetary Exploration Research Center, Chiba Institute of Technology, Narashino 275-0016, Japan.
3. Kochi University, Kochi 780-8520, Japan.
4. Nagoya University, Nagoya 464-8601, Japan.
5. Rikkyo University, Tokyo 171-8501, Japan.
6. Institute of Space and Astronautical Science (ISAS), Japan Aerospace Exploration Agency (JAXA), Sagamihara 252-5210, Japan.
7. University of Aizu, Aizu-Wakamatsu 965-8580, Japan.
8. National Institute of Advanced Industrial Science and Technology, Tokyo 135-0064 Japan.
9. Kobe University, Kobe 657-8501, Japan.
10. Meiji University, Kawasaki 214-8571, Japan.
11. National Astronomical Observatory of Japan, Mitaka 181-8588, Japan.
12. SOKENDAI (The Graduate University for Advanced Studies), Hayama 240-0193, Japan.
13. Planetary Science Institute, Tucson, AZ 85719-2395, USA.
14. Auburn University, Auburn, AL 36849, USA.
15. Tohoku University, Sendai 980-8578, Japan.
16. Brown University, Providence, RI 02912, USA.
17. Kindai University, Higashi-Hiroshima 739-2116, Japan.

18. Université Côte d'Azur, Observatoire de la Côte d'Azur, Centre National de le Recherche Scientifique (CNRS), Laboratoire Lagrange, 06304 Nice, France.
19. University of Arizona, Tucson, Arizona 85705, USA.
20. Johns Hopkins University Applied Physics Laboratory, Laurel, MD 20723, USA.
21. German Aerospace Center (DLR), Inst. of Planetary Research, Berlin 12489, Germany.
22. International Research School of Planetary Sciences, Università d'Annunzio, Pescara 65127, Italy.
23. Ashikaga University, Ashikaga 326-8558, Japan.
24. Hokkaido University of Education, Asahikawa 070-8621, Japan.
25. Max-Planck-Institut für extraterrestrische Physik, Garching 85748, Germany.
26. University of Stirling, FK9 4LA, Scotland, UK.
27. Research and Development Directorate, JAXA, Sagamihara 252-5210, Japan.
28. Nihon University, Funabashi 274-8501, Japan.
29. Osaka University, Toyonaka 560-0043, Japan.
30. Hitotsubashi University, Tokyo 186-8601, Japan.
31. Hiroshima University, Higashi-Hiroshima 739-8526, Japan.
32. Seoul National University, Seoul 08826, Korea.
33. NASA Johnson Space Center, Houston, TX 77058, USA.
34. Laboratoire d'Etudes Spatiales et d'Instrumentation en Astrophysique (LESIA)-Observatoire de Paris, Paris Sciences et Lettres (PSL), Centre National de le Recherche Scientifique (CNRS), Sorbonne Univ., Univ. Paris-Diderot, 92195, Meudon Principal Cedex, France.

*Corresponding author: E-mail: sugita@eps.s.u-tokyo.ac.jp
†Current affiliation: National Institute for Environmental Studies, Tsukuba 305-8506, Japan.
‡Current affiliation: Mitsubishi Electric Corporation, Kamakura 247-8520, Japan.
§Deceased.

Abstract: The Hayabusa2 spacecraft obtained global multi-color images of the near-Earth carbonaceous asteroid 162173 Ryugu, which is believed to have been born from a parent body that accreted substance containing water ice and organics. Geomorphological features present on Ryugu include a circum-equatorial ridge, east/west dichotomy, high boulder abundances across the entire surface, and impact craters. Age estimates from the craters indicate a resurfacing age of $\lesssim 10^6$ years for the top 1-meter layer. Ryugu is among the darkest bodies in the Solar System. The high abundance and spectral properties of boulders are consistent with moderately dehydrated materials, as analogous to thermally metamorphosed meteorites found on Earth. The general uniformity in color across Ryugu's surface supports partial dehydration due to internal heating of the asteroid's parent body.

One Sentence Summary: The rapidly resurfaced Ryugu surface is low in albedo and hydration and full of boulders with multiple lithologies.

Main Text:

The asteroid 162173 Ryugu is the target of JAXA's Hayabusa2 mission, which arrived in June 2018. Small asteroids, such as Ryugu, are estimated to have been born from much older parent bodies through catastrophic disruption and re-accumulation of fragments during the Solar System evolution (1, 2). We seek to understand the properties of both Ryugu and its parent body.

Deciphering the geologic record of an asteroid requires identification and characterization of the geological features on its surface. Detailed global observations of Ryugu were conducted with Hayabusa2's remote-sensing instruments, including the optical navigation cameras (ONC), including the nadir-viewing telescopic camera (ONC-T), with seven narrow-band filters (0.40 μm (ul), 0.48 μm (b), 0.55 μm (v), 0.59 μm (Na), 0.70 μm (w), 0.86 μm (x), and 0.95 μm (p)) (3-5), a laser altimeter (LIDAR) (6), and a thermal infrared camera (TIR) (7), sensitive to wavelengths from 8 to 12 μm (8).

Global images were obtained from 'Home Position' located 20 km above the asteroid (9), from which we constructed a 0.55-μm map of Ryugu (Fig. 1A). Major geomorphologic features visible in this map include impact craters, boulders, troughs, and an equatorial ridge(Fig. 1B, Table S3).

Impact craters

Impact crater morphologies, including rim and floor characteristics, provide indicators of surface age and mechanical properties. Approximately 30 circular depressions ≥20 m in diameter have been identified on Ryugu, many (at least half) with raised rims (Fig. 1A). Several craters also exhibit bowl-like shapes (Fig. 2A and 2B), while others have shallow floors (Fig. S10). The bowl-shaped depressions are classified based on rim morphology and shape, providing confidence levels (CLs) to their identification as impact craters. CL1 features are circular with a clearly identifiable rim, CL2 depressions are circular but exhibit no rim, and CL3 depressions are quasi-circular. CL1 and CL2 depressions are most likely impact craters. The group of CL3 depressions may include a few craters. Different levels of confidence are used in the statistical analyses to examine the robustness of the results. Laser-altimeter measurements indicate that fresh bowl-shaped depressions have depth/diameter ratios ranging from 0.14 – 0.2 (Figs. 2C and 2D, 8). Although recent numerical calculations (10) show that large cavities may be formed in fast-spinning asteroids via the release of large boulders due to centrifugal force, raised rims are not expected to be generated in such a process. Thus, large equatorial craters on Ryugu are unlikely to have been formed by asteroid spin and are most likely of impact origin.

Some craters show evidence for motion of loosely consolidated mass of materials on the inner walls (i.e., wall slumping, Fig. 2A). This was not observed on another sub-kilometer asteroid Itokawa (11) and indicates the presence of an unconsolidated surface layer. No crater has been found to have a floor with terrace structure, which would form if there was a large strength contrast between the surface and near-surface interior (12). These floor morphologies and the high fraction of raised rims indicate the craters formed in an unconsolidated target, not dominated by pristine mechanical strength of the constituent surface material. Therefore, both gravity and weak cohesion strength controlled the crater formation. Furthermore, the sizes of individual boulders in the surface layer are large (~3 m in diameter) and similar to the sizes of the projectiles (~0.1 – 1 m) that formed craters (~1 – 30 m) on Ryugu (8). Thus, these large boulders may reduce crater size via armoring, in which a large fraction of impact energy is lost into the crushing or cratering of the first-contact boulder instead of forming a granular crater on the asteroid (13). Impact experiments using targets with constituent boulder sizes similar to the projectile's size indicate that armoring effects influence crater size, and that a scaling relation for such targets must include a term for the breakup energy of the first-contact target boulder (14).

We estimated the surface crater retention age based on the number density of craters 100 – 200 m in diameter, using a scaling rule with armoring effect (14), both with and without a dry-soil cohesion factor, obtaining surface ages of 10^8 and 10^7 years, respectively (Fig 2E, 8). This

large (i.e., a factor of ten) uncertainty in surface age comes from the influence of a small amount of cohesion, which controls the excavation flow near the crater rim. On a high-gravity planet, such as Earth, small cohesive forces do not influence the crater size, but on micro-gravity bodies, such as Ryugu, crater size is influenced by the presence or absence of small cohesive forces, which is difficult to simulate in laboratory experiments on Earth. Despite these uncertainties, the observed crater size frequency distribution (CSFD) indicates that the surface age of Ryugu is equal to or younger than the collisional lifetime, during which an asteroid experiences a collision-induced catastrophic disruption on average, of kilometer-sized objects in the main asteroid belt ($3 – 5 \times 10^8$ years (1, 2)) and equal to or older than the expected time ($\sim 4 \times 10^7$ years) Ryugu has stayed in a near-Earth orbit (9). Here different collision frequencies need to be considered for different scales of surface ages because Ryugu is estimated to have migrated from the main belt to the near-Erth orbit most likely through ν_6, the inner most resonance zone of the main belt (9, 15). Because the collision frequency is far greater in the main belt, the majority of the craters ≥100 m probably formed while Ryugu was still resident in the main asteroid belt.

Ryugu's CSFD shows a deficit of small craters (< 100 m, Fig. 2F). The deficit of small craters on Ryugu as a function of crater size is similar to that found for both Itokawa and Eros (16). Because craters in this size range on Ryugu are not greatly influenced by crater size reduction (because of armoring effects (14)), these depletion patterns are more likely to be due to crater erasure processes, such as seismic shaking (16). The reduced number of small craters (< 100 m) indicates that the crater retention time in this size range is very young. The number density of craters ~ 10m indicates that the average resurfacing of the top ~1-meter layer on Ryugu is $<10^6$ years for the main belt impact flux (Fig 2F) and $< 2\times10^6$ years for near-Earth impact flux (Fig. S3). Because impact cratering is a stochastic process, some of these small craters must have formed more recently, exposing fresh material.

Mass wasting

There is abundant evidence for mass movement along slopes (i.e., mass wasting) on Ryugu, particularly around the equatorial ridge and several craters, such as Urashima crater (Fig. 2A). Some groups of boulders observed along the equatorial ridge are overlapping one another with preferred orientations (i.e., imbrication) away from the ridge, and they are accompanied by asymmetrically distributed fragmental debris deposits (i.e., regolith). The edges of these boulders display little to no regolith deposits along the downhill sides of the ridge (Fig. 1C). Such imbrication typically occurs during landslides. The asymmetric regolith deposits along these boulders indicate that the direction of recent mass wasting is from the top of the equatorial ridge towards higher latitudes, consistent with Ryugu's current geopotential (9, 17). Wall slumping is observed along crater walls, as discussed above (e.g., Fig. 2A). Some craters, such as Momotaro (12.5ºN, 51.9ºE) near the equatorial ridge, exhibit a higher concentration of large boulders on their floors than on their rims and walls (Fig. S8). Such preferential concentration of larger boulders in topographic lows also occurs as a result of mass wasting. These observations suggest that the equatorial ridge is made of mechanically unconsolidated materials and may have been formed during a period of rapid spin (17), as material flowed towards an equatorial topographic low. An unconsolidated nature would have allowed Ryugu to reshape, perhaps in response to a change in spin rate. When Ryugu was established in its current geopotential configuration, the ridge experienced mass wasting as some of the unconsolidated materials flowed toward new topographic lows at higher latitudes. Furthermore, interior walls in large craters, such as Urashima, exhibit evidence for mass wasting, such as imbricated boulders and run-up deposits

(Fig. S8B). This indicates that mass wasting postdates these large craters, which were formed after equatorial ridge.

Disk-averaged color

During Hayabusa2's approach phase (prior to arrival and parking at Home Position) a series of disk-averaged photometric observations were acquired in each of the seven ONC filters over twelve different rotational phases. We used these data to examine the accuracy of the radiometric calibrations of ONC-T for each filter. Global reflectance values from the ONC-T images based on pre-flight and in-flight calibrations (3-5) were compare with ground-based photometric and spectral observations at 0.55 μm (18). The results were consistent within the uncertainties, validating that ONC-T appropriately calibrated over all filters (5, 8).

The disk-averaged 7-band color measurements exhibit little variation (< 0.5%) over the different rotational phases observed (Fig. 3A). The color properties are consistent with the classification of Ryugu as a Cb-type asteroid based on the Bus taxonomy (19). This spectral type establishes connections with potential main belt asteroid families and Ruygu's parent body. Some ground-based spectral observations have suggested the presence of hydrated minerals, due to spectral features observed at 0.7 μm and <0.55 μm (20-22). This would imply that Ryugu's parent body could be a Ch-Cgh asteroid, similar to the Erigone asteroid family (23). However, the ONC-T color observations rule out such a parent body, as do results from Hayabusa2's Near-InfraRed Spectrometer (NIRS3), which show Ryugu's globally averaged near-infrared spectrum does not have any strong OH absorption band signature around 2.8 μm; only a weak absorption band is seen at 2.72 μm (24).

The observed visible spectral type is close to that of the asteroids Eulalia and Polana, which parent bodies of C-complex asteroid families in the inner main belt (25).The asteroid Erigone has different spectral type (Fig. 3A). Orbital dynamics calculations have shown that the most likely origin of Ryugu is either Eulalia or Polana (15). The collisional lifetime of Ryugu (3 – 5 × 10^8 yr) is similar to or less than the breakup time of these families (830^{+370}_{-150} My and 1400 ± 150 Myr for Eulalia and Polana, respectively (15)). Ryugu may not be composed of material directly ejected from one of these large bodies, but could be the product of more than one generation of disruption.

The link between Ryugu and Cb asteroids in the inner main belt has implications for possible meteorite analogues. The fraction of Cb- to B-type asteroids in the main asteroid belt high; Fig. S6 indicates that about half of the C-complex asteroids in the main belt are of types Cb, B, and C, which do not display a clear 0.7-μm band. Their populations in the inner main belt, from which the largest fraction of Near-Earth asteroids is derived (2), contains many large families, such as Eulalia and Polana, with these spectral characteristics (23). Therefore, the B-Cb-C population comprises a large fraction of the material reaching Earth as meteorites. There are two major candidates for Ryugu meteorite analogues with sufficiently low-albedo materials: thermally metamorphosed carbonaceous chondrites (26, 27), or interplanetary dust particles (IDPs). The latter consist of highly primitive material that has experienced no (or only weak) water-rock reaction to form hydrated silicates (28, 29).

Albedo and reflectance

We used the point-source and whole-disk observations of Ryugu to characterize the disk-integrated photometric phase behavior in all seven ONC-T filters using Hapke modelling (Table S1, 8). Based on these photometric measurements, we derived a geometric albedo of (4.5 ± 0.2)

% at 0.55 μm, similar to typical comets (30) and the darkest asteroids, such as 253 Mathilde, another Cb-type asteroid (19, 31). We derived the disk-integrated surface reflectance at the standard laboratory observation angles (i, e, α = 30°, 0°, 30° where i, e, and α are incident, emission, and solar phase angles, respectively), for comparison with meteorite samples measured in the laboratory.

The standard-condition reflectance is (1.60 ± 0.15) % at 0.55 μm, which is lower than any meteorites reported in the literature. The darkest published meteorite samples are the thermally metamorphosed carbonaceous chondrites (26, 32). Recent measurements of this type of meteorites, such as Jbilet Winselwan, Y 86029, and Y-793321, exhibit reflectance comparable to Ryugu (Fig. 3B). Those meteorite samples belong to the moderate heating stages II and III groups of meteorites, in which hydrated silicates have been altered into amorphous silicates due to dehydration, but have not recrystallized into olivine or pyroxene (33). Most of these samples are powders; rough slab surfaces, such as Ryugu's surface, generally exhibit lower reflectance and bluer spectra. Although spectral data of slab samples are not as frequently reported as powder samples, slab spectra of major carbonaceous chondrites from each clan, such as Murchison and Mighei for CM and Ivuna for CI, have been measured (34, 35). These slab samples are not consistent with Ryugu's spectrum.

Local color variation and age-color relation

Surface colors at specific locations on Ryugu span a large range, consistent with the colors of C-complex asteroids (Fig. 3). The vast majority of Ryugu's surface has colors we denote "typical regolith" (Figs. 3C-D). Other color types are found in relatively limited areas and/or geological features on Ryugu, such as distinctive boulders and crater bottoms. Thus, we analyze the color of all the pixels on Ryugu with small incidence i and emission e angles ($i \leq 40°$ and $e \leq 40°$) and use them to define the regolith color variation across the surface.

The general spectral slope from b-band (0.48 μm) to x-band, (0.86 μm) exhibits the greatest regional variation; Ryugu's surface has bluer spectral slopes at both poles, on the equatorial ridge, and in large troughs (Fig. 3E). Both polar regions and the equatorial ridge are topographic highs, which may be subject to gradual erosion, leading to the exposure of fresh surface material. Steep boulder surfaces, which may be experiencing recent erosion by thermal fatigue (36) or other processes, tend to have brighter and bluer surfaces (Figs. 3C-D). In contrast, many locations conducive to deposition, such as crater floors, exhibit redder and darker colors. These observations suggest that exposure of Ryugu materials to space leads to their reddening and darkening. It is not clear if this trend is because of space weathering or other processes, such as coating of redder/darker dust (8). Local-scale heterogeneity suggests that the large-scale uniformity may not be due to pristine materials on Ryugu's surface, but instead may be the result of a well-mixed surface.

No regolith-covered surface on Ryugu exhibits a strong 0.7-μm absorption in the ONC-T color data. Dynamical calculations have shown that many Near-Earth Objects (NEOs) experienced dehydration during orbital excursions near the Sun, which may have contributed to the depletion in 0.7-μm absorption in C-complex NEOs (37). NEOs with Ryugu-like orbits may experience large orbital excursions on a time scale of 10^7 years, and the skin depth of solar heating during Ryugu's orbital evolution is tens of centimeters (9). This timescale is longer than the retention age ($< 2 \times 10^6$ years) of 10-m craters, which excavate unheated substrate material (crater depths ~1 m). Thus, the lack of a high degree of hydration on Ryugu is unlikely to be due to solar heating during a recent orbital excursion.

West/East dichotomy

Ryugu's western side (160°E – 290°E), which is surrounded by troughs (Figs. 1A, B), has a v-band albedo higher than other areas (Figs. 3F, S13). This western side also has a lower number density of large boulders (Fig. 4A). The topographic highs and bluish b-x spectral slope of the equatorial ridge transect the troughs, suggesting that the equatorial ridge formed more recently than the troughs. Although the equatorial ridge has depressions around 160°E and 290°E in longitude, these have morphologic characteristics more consistent with impact craters, so we do not consider them to be connected to the mass motion that formed the trough. The formation of the east/west dichotomy probably predates the equatorial ridge formation. However, because there is no difference in b-x spectral slope between the western side and other regions on Ryugu, the nature of its enhanced reflectance is probably is not the result of a shorter exposure to the space environment. In contrast, the coincidence between high v-band reflectance and low boulder abundance suggests that this dichotomy may be reflecting smaller grain size in the western hemisphere. The two hemispheres may have different physical properties, such as grain size and mobility. Such different states could be resulting from re-accumulation of two large bodies of rubble piles with different grain sizes during the re-accumulation stage immediately after the catastrophic disruption of the parent body.

Principal-component analysis

We conducted a principal-component analysis (PCA) to the ONC-T filter data and the second phase of the Small Main-belt Asteroid Spectroscopic Survey (SMASSII) observations of C-complex main belt asteroids by ground-based telescopes. This method has been used widely for asteroid spectral analysis and has served as a basis for spectral type definitions (19, 38). Because most reflectance data registered in SMASSII covers only 0.43 μm to 0.9 μm, we limited the ONC-T data to the b to x bands, excluding the ul and p bands centered at 0.39 μm and 0.95 μm. Because PCA can expand spectra into orthogonal basis functions, PCA often extracts linear combinations of spectra with physical/mineralogic meanings as the principal components (PCs). Non-orthogonal linear combinations of the second and third PCs produced by our analysis (PC2 and PC3) correspond to the 0.7-μm absorption and drop-off in reflectance shortward of v-band (Figs. 5B and S5). Our results indicate that regolith spectra from ONC-T are consistent with moderately dehydrated carbonaceous chondrites (e.g., Y 86029), and reside both near the edge of the B-Cb-C population and the dehydration tracks for CM/CI chondrites (Figs. 5B and S4).

TIR observations provide constraints on surface grain size, which influences the PCA results of colors on Ryugu. TIR observations indicate that the peak temperatures of Ryugu's surface correspond to uniform thermal inertia values between 200 to 500 $Jm^{-2}s^{-0.5}K^{-1}$ (Fig. 6). These values are consistent with the disk-averaged value (150 to 300 $Jm^{-2}s^{-0.5}K^{-1}$) estimated based on pre-arrival telescope observations (39) and suggest sub-cm to 10-cm grains (7, 40); the fraction of surface area covered with grains ≤1 mm is very small. Laboratory examination of carbonaceous chondrite powders of different grain sizes demonstrates that in the visible wavelengths the reflectance and the spectral slope do not greatly change for grain sizes greater than ~1 mm, although the effects of compaction and thin coating of fine powers may influence the spectra (41). Comparison between the PCA results of Ryugu's surface and the dehydration track for heated coarse-grained samples of the Murchison meteorite show that the distribution of Ryugu's surface is much narrower than that of the Murchison dehydration track in the PC space

(Fig. 5B), suggesting that Ryugu is dominated by materials experienced similar degrees of dehydration.

Abundance and distribution of boulders

There are large numbers of boulders across Ryugu's surface, with a wide size range (Fig. 4B). The largest boulders (> 20 m) are too large to be ejecta from the observed craters (≤ 300 m) (42), suggesting they are fragments from Ryugu's parent body. The cumulative distribution of boulder sizes follows a power law with an exponent between -2.5 and -3 (Fig. 4B), similar to that measured for other small asteroids (43-45).

The global average number density of boulders ≥20 m in diameter at latitudes ≤70° is 50 km^{-2}. This is more than twice that on Itokawa (39, 41). However,the number density of craters on Ryugu is of the same order of magnitude as Itokawa, which suggests that boulders on both asteroids have experienced similar degrees of meteoritic bombardment. Thus, the higher abundance of large boulders on Ryugu suggests that these boulders may have impact strength of a similar order of magnitude to those on Itokawa. Given the apparent high surface mobility, it is possible that many of them may have been ejected from Ryugu to space as macroscopic bodies. This leads to the possibility that fragments from Ryugu may reach the Earth as macroscopic meteorites.

The spatial distribution of boulders on Ryugu is different from that on Itokawa and Eros, which have boulder-poor regions, such as smooth terrains (46, 47) and regolith ponds (48). Ryugu does not have large areas with low boulder abundance, suggesting that the degree of size sorting is much lower on Ryugu. A contributing factor may be the difference in the overall shape of these asteroids: Itokawa and Eros are elongated while Ryugu is spheroidal. However, there is evidence for some global size segregation in the latitudinal variation in boulder size: the boulder number density is lower in the equatorial region than at higher latitudes (Fig. 3A). This may be because of mass flow during the equatorial ridge formation (17). There is also a smaller boulder abundance variation in the longitudinal direction (Fig. 3B), with the boulder abundance in the western hemisphere (160° – 290° in East longitude) systematically lower than at all other longitudes on Ryugu.

Color and morphology of boulders

There is a systematic trend between boulder colors and morphologies on Ryugu. We have identified four distinct morphologic boulder types: (Type 1) Dark and rugged boulders. This type possesses rugged surfaces and edges, tends to have uneven layered structures possibly related to inclusion of coarse-grained clasts (Figs. 4C and S11A), and has color properties similar to Ryugu's average color (Fig. 3C). Many boulders of this type are partially buried by regolith, such as Ejima Saxum (Fig. 1A). (Type 2) Bright and smooth boulders. This boulder type displays many thin and parallel layers (Fig. 4D), many are emplaced on the top of the regolith, and some exhibit distinctive striped patterns (Fig. S11B). Their typical color ranges from slightly bluer than average to Ryugu's average color (Fig. 3). (Type 3) Bright and mottled boulders. This boulder type does not show clear layers but displays a blocky variegation in albedo (Figs. 4E and S11C). Their bright parts exhibit a drop-off in reflectance at short wavelengths (ul and b) (Fig. 3C). (Type 4) The largest boulder on Ryugu, Otohime Saxum, does not match the other types. It is located near the south pole (Figs. 1 and 4F), with sharp edges and smooth surfaces but no obvious layering. Its vertical face is the brightest surface on Ryugu and exhibits a very blue color

(Fig. 3). The differences in brightness among these four types of boulders are not very large; the range of their v-band reflectance factor is similar to that of the background regolith (Fig. 5A).

More quantitative examinations of boulder colors were performed using reflectance/slope statistics and PCA. Although the dark rugged and bright smooth boulders are distinct in morphology, they form a single linear trend in reflectance/slope diagrams and PC2-PC3 space (Fig. 5) parallel to the general distribution of PC scores over the entire surface. The range in boulder color variation is similar to the color variation seen over the entire surface; the range of PC2 scores of 27 large boulders encompasses the PC2 score range of more than half of Ryugu's surface. This agreement in PC-score trends between regolith and boulders suggests that the color variation in regolith on Ryugu may be controlled by the color variation of these two types of boulders, from which the regolith may be produced through comminution processes.

In contrast, the different sides or facets of the Otohime Saxum form their own trend in the reflectance-slope diagram (Fig. 5A) and PC spaces (Figs. 5B and S7), approximately parallel to the trend for heat-induced dehydrated carbonaceous chondrite materials (26). Figs. 5B and S4 show that the trend found in Otohime Saxum is also parallel to the distribution trend in the B-Cb-C population, suggesting that their color variations may result from the same process, such as dehydration. ~~Figs. 5B and S4 show that the trend obtained by (26) is parallel to the dividing line between two populations of C-complex asteroids, those with and without the 0.7 μm absorption band, as shown by (19).~~

In the PC2-PC3 space, the bright mottled boulders are consistent with the Ch-Cgh asteroid population, closest to Erigone (Fig. 5B). These type 3 boulders extend the trend seen in the regolith other types of boulders (Figs. 5B and S7). The 0.7-μm absorption, measured as the difference, $(v+x)/2w - 1$, between w-band reflectance and the linear continuum defined by v- and x-band reflectance values, is not stronger than the average Ryugu spectrum. Type 3 boulders are close in PC space to the Ch-Cgh population due to their low b-band reflectance.

The linear trend extending through type 3 boulders, the average regolith and type 1 and 2 boulders is seen in the first three PC values plotted against albedo. This trend cannot be produced by space weathering and/or grain size effects. It is also different from the L-shaped distribution of laboratory dehydration data (Fig. 5B). Although the low-temperature evolution of the dehydration track for CM chondrites is similar to the boulder trend (both cross the dividing gap between Ch-Cgh and B-Cb-C populations and have a large PC2 change), they differ in PC3 change, leading to a very different slope in the PC2-3 space. Instead, the trend formed by the boulder types 1-3 connects the average Ryugu spectrum and the Ch-Cgh population. A simple interpretation of these trends is the mixing between two components in Ch-Cgh and B-Cb-C populations. This trend is consistent with mixing seen not only in the regolith but also in the boulders. This observation based on PCA suggests that these boulders have experienced mixing processes.

Boulder texture and regolith grains

Hayabusa2 carried several landers (MIcro Nano Experimental Robot Vehicle for Asteroid (MINERVA-IIs) and Mobile Asteroid Surface Scout (MASCOT)). Deployment of these landers required multiple spacecraft descents down to <100 m altitude, which provided opportunities for obtaining close-up images down to 6-mm pixel scale (Figs. 7 and S14).

The higher resolution images show the global size distribution of both boulders and pebbles follows a power-law distribution down to decimeter scales; the slope (i.e., power-law index) of their cumulative size distribution is about –2.5 at sizes larger than ~0.2 m, similar that

found for large blocks (10 – 160 m) (Fig. 4B). Then, the slope becomes shallower at smaller sizes (Fig. S14A). The shallower slope in the small size range suggests a non-negligible mechanical strength to individual boulders/pebbles on Ryugu. Although such high-resolution measurements have been conducted only in limited areas on Ryugu, no differences have been seen between areas outside on and off the equatorial ridge.

Many images of Ryugu exhibit bright spots (Figs. 7A, 7B, and S14B). Some of these spots are brighter than the average background by a few tens of percent, while others are brighter by a factor of two or greater. These spots may be impact craters or recent fragments from preexisting boulders, both of which could exhibit higher albedos because of the freshness of their interior, or they may be small fragments of distinct intrinsic composition. Their distinctive brightness and relatively low abundance suggest they may be made of materials similar to bright and mottled boulders, whose spectra are consistent with Ch-Cgh populations (Fig. 5). Ryugu's surface material may be a mixture of materials with different lithologies representative of its parent body.

Heterogeneity in brightness can also be found within individual boulders (Fig. 7A). This morphologic characteristic is consistent with coarse-grained clastic rocks (impact breccia) including rock fragments broken by impact. The majority constituent of carbonaceous chondrites has been proposed to be impact breccia (49). This suggests material mixing before these boulders were formed, which likely took place on Ryugu's parent body. Because impact breccias can contain multiple components with variable mixing ratios, they can readily account for the mixing trends seen in the PC spaces (Fig. S7). Breccia formation on the parent body can also account for porous textures seen in many dark boulders on Ryugu (Fig. 7B). These porous boulders seen in the high-resolution images have the same morphologies as the dark/rugged boulders observed in lower resolution global/regional images (Fig. 4C). These boulders often have quasi-parallel layers (Fig. 7B). Thus, if these boulders are impact breccias, they may originate from the sedimentation of multiple ejecta blankets.

Layered structures are seen on boulder surfaces, suggesting that these boulders are not covered with loose regolith, supporting our interpretation that the thermal inertias of boulders measured by TIR (Fig. 6) reflect the bulk properties of the boulders. The presence of rugged grains and pores is also consistent with low thermal conductivity and density.

The porous nature of impact breccias would increase the bulk porosity of Ryugu. The very low bulk density ($(1.19 \pm 0.02) \times 10^3$ kg/m^3) of Ryugu would require very high porosity (~50%) if the grain densities of typical carbonaceous chondrites are assumed (17). Such a high porosity is substantially more than that (~40%) for closest packing with a single boulder size. If Ryugu possesses pores within individual boulders (i.e., intra-boulder pores) in addition to pores between multiple boulders (i.e., inter-boulder pores), such low density can be achieved with typical carbonaceous chondrite materials.

Implications for the evolution of Ryugu's parent body

Our observations suggest the presence of partially hydrated minerals on Ryugu, though with a low degree of hydration. The low average albedo (Fig. 3B), average spectra lying in the midrange on dehydration tracks of CM and CI chondrites (Fig. 5B), and the shortward drop off in the spectra of some boulders (Fig. 3D) are consistent with moderately dehydrated carbonaceous chondrites (CCs) and/or weakly altered IDPs, and inconsistent with completely dehydrated CCs. In this section, we discuss the origin of these materials on Ryugu.

Recent numerical calculations of large asteroid breakups by collision show that fragments formed by the re-accumulation of material, resulting in a rubble pile structure, can contain materials sampling different depths on the original parent asteroid (~100 km in diameter) (50). Mixtures of impact debris with different lithologies from the original parent body could deposit on the reaccumulated fragments, leading to the formation of impact breccias. A subsequent impact on such a reaccumulated fragment would generate boulders with a large heterogeneity in color properties. Using a similar method, we conducted numerical calculations to estimate how much material is collected in reaccumulated bodies from different depths from a 100-km diameter parent body (8, Fig. S9). The results indicate that materials from all depths of the parent body are accumulated in each small re-accumulated body. This could account for both the relatively homogeneous spectral properties of Ryugu and the limited amount of local heterogeneity found in the boulders. if partial dehydration occurred as a result of internal heating, e.g. due to radioactive decay of ^{26}Al. Internal heating can warm a large fraction of the volume of the parent body relatively uniformly, leaving a small volume of outer layer relatively cool (51, Fig. 8).

In contrast, partial dehydration due to a single-shock heating event, such as that induced by the catastrophic impact that disrupted the original parent body, is unlikely because the vast majority of boulders on Ryugu do not possess a strong 0.7-μm absorption band. In order to suppress the 0.7-μm band in the vast majority of a resulting reaccumulated fragments body, the impact has to heat up the relevant mass to 400°C or higher. However, impact heating is an inefficient global process; efficient heating occurs only around the impact site (Fig. S15). Most of the volume does not experience much heating and simply fractures into cold impact fragments. The numerical calculation results (50, Fig S9) indicate that a catastrophic disruption event due to a large impact would sample different portions of the parent body along the excavation streamlines. Thus, fragments re-accumulating to form a reaccumulated fragments body would be very heterogeneous unless the parent body itself was homogeneous i.e. the large-scale radial heterogeneity in the parent body would be inherited by the boulders comprising the reaccumulated fragments body. Consequently, the preponderance of materials with little water signature on Ryugu suggests that a dominant part of its original parent body was also water poor. Such global partial dehydration is possible with impacts, but only if there were many impacts before the catastrophic disruption (Fig. 8). Geochemical analyses of thermally metamorphosed meteorites are consistent with short-term heating (27, 52); thus, this scenario cannot readily be discarded. However, the observation that Ryugu's regolith and boulders are concentrated in a relatively small area in the dehydration track in the PC spaces suggests that a large volume of Ryugu's original parent body was dehydrated to a similar state. Such uniformity is more consistent with internal heating on the parent body than partial dehydration caused by multiple impacts.

An alternative possibility is that Ryugu is covered with materials that experienced only incipient aqueous alteration before forming Fe-rich serpentine, which has 0.7-μm absorption. In this scenario, the closest meteoritic counterpart would be IDPs. If Ryugu is made of such highly primitive materials, the trend connecting regolith/dark boulders in the B-Cb-C population and bright/mottled boulders in the Ch/Cgh population may be a progression of aqueous alteration (28, 29). However, there are insufficient IDPs reflectance spectra available to constrain this scenario. It is difficult to distinguish materials that experienced a low degree of hydration from originally highly hydrated materials that experienced partial dehydration. Nevertheless, the boulders on Ryugu have survived impact processes during catastrophic disruption, the re-

accumulation process, and more recent impacts on Ryugu; they are not dust balls with little cohesion. Thus, this scenario is in conflict with the boulder-rich nature of Ryugu. If Ryugu is composed of IDP-like materials and does not have a macroscopic meteorite counterpart, there must be an additional mechanism to break up boulders and pebbles before arriving at Earth as meteorites.

Although multiple scenarios for the evolution of Ryugu's parent body remain viable, our comparison between Hayabusa2 remote-sensing data, meteoritic samples and asteroids leads us to prefer the scenario of parent-body partial dehydration due to internal heating. This scenario suggests that asteroids that accreted materials condensed at ≤150 K, where H_2O condensation temperature under typical solar nebula conditions, must have either formed early enough to contain high concentrations of radiogenic species, such as ^{26}Al, close to the Sun where they experienced other heating mechanisms (53). The degree of internal heating would constrain the location and/or timing of the snowline (i.e., the dividing line between H_2O condensation and evaporation) in the Solar System.

References and Notes:

1. D. P. O'Brien, R. Greenberg, The collisional and dynamical evolution of the main-belt and NEA size distributions. *Icarus* **178**, 179–212 (2005). doi: 10.1016/j.icarus.2005.04.001
2. W. F. Bottke et al., The fossilized size distribution of the main asteroid belt. *Icarus* **175**, 111–140 (2005). doi: 10.1016/j.icarus.2004.10.026
3. S. Kameda et al., Preflight calibration test results for optical navigation camera telescope (ONC-T) onboard the *Hayabusa2* spacecraft. *Space Sci. Rev.* **208**, 17–31 (2017). doi: 10.1007/s11214-015-0227-y
4. H. Suzuki et al., Initial inflight calibration for Hayabusa2 optical navigation camera (ONC) for science observations of asteroid Ryugu. *Icarus* **300**, 341–359 (2018). doi: 10.1016/j.icarus.2017.09.011
5. E. Tatsumi et al., Updated inflight calibration of Hayabusa2's Optical Navigation Camera (ONC) for scientific observations during the cruise phase. *Icarus* **325**, 153–195 (2019). doi: 10.1016/j.icarus.2019.01.015
6. T. Mizuno et al., Development of the laser altimeter (LIDAR) for Hayabusa2. *Space Sci. Rev.* **208**, 33–47 (2016). doi: 10.1007/s11214-015-0231-2
7. T. Okada et al., Thermal Infrared Imaging Experiments of C-Type Asteroid 162173 Ryugu on Hayabusa2. *Space Sci. Rev.* **208**, 255–586 (2017). doi: 10.1007/s11214-016-0286-8
8. Materials and Methods are available as Supplementary Materials.
9. S. Tardivel et al., Equatorial cavities on asteroids, an evidence of fission events. *Icarus* **304**, 192–208 (2018). doi: 10.106/j.icaus.2017.06.037
10. P. Michel, M. Delbo, Orbital and thermal evolutions of four potential targets for a sample return space mission to a primitive near-Earth asteroid. *Icarus*, **209**, 520–534 (2010). doi: 10.1016/j.icarus.2010.05.013
11. N. Hirata et al., A survey of possible impact structures on 25143 Itokawa. *Icarus* **200**, 486–502 (2009). doi: 10.1016/j.icarus.2008.10.027
12. V. R. Oberbeck, W. L. Quaide, Genetic Implications of Lunar Regolith Thickness Variations. *Icarus* **9**, 446–465 (1968). doi: 10.1016/0019-1035(68)90039-0

13. C. Güttler, N. Hirata, A. M. Nakamura, Cratering experiments on the self armoring of coarse-grained granular targets. *Icarus* **220**, 1040–1049 (2012). doi: 10.1016/j.icarus.2012.06.041
14. E. Tatsumi, S. Sugita, Cratering efficiency on coarse-grain targets: implications for the dynamical evolution of asteroid 25143 Itokawa. *Icarus* **300**, 227–248 (2018). doi: 10.1016/j.icarus.2017.09.004
15. W. F. Bottke et al., In search of the source of asteroid (101955) Bennu: Applications of the stochastic YORP model. *Icarus* **247**, 191–217 (2015). doi:10.1016/j.icarus.2014.09.046
16. P. Michel, D. P. O'Brien, S. Abe, N. Hirata, Itokawa's cratering record as observed by Hayabusa: Implications for its age and collisional history. *Icarus* **200**, 503–513 (2009). doi: 10.1016/j.icarus.2008.04.002
17. S. Watanabe et al., Hayabusa2 observations of the top-shape carbonaceous asteroid 162173 Ryugu. *Science*, this issue (2019).
18. M. Ishiguro et al., Optical properties of (162173) 1999 JU3: In preparation for the JAXA Hayabusa2 sample return mission. *Astrophys. J.* **792**, 74 (2014). doi:10.1088/0004-637X/792/1/74
19. S. J. Bus, R. Binzel, Phase II of the small main-belt asteroid spectroscopic survey. A feature-based taxonomy. *Icarus* **158**, 146–177 (2002). doi: 10.1006/icar.2002.6856
20. R. P. Binzel et al., Spectral Properties of Near-Earth Objects: Palomar and IRTF Results for 48 Objects Including Spacecraft Targets (9969) Braille and (10302) 1989 ML. *Icarus* **151**, 139–149 (2001). doi: 10.1006/icar.2001.6613
21. F. Vilas, Spectral characteristics of Hayabusa 2 Near-Earth asteroid targets 162173 1999 JU3 and 2001 QC34. *Astron. J.* **135**, 1101–1105 (2008). doi:10.1088/0004-6256/135/4/1101
22. D. Lazzaro et al., Rotational spectra of (162173) 1999 JU3, the target of the Hayabusa2 mission. *Astrophs. Astron.* **549**, L2 (2013). doi: 10.1051/0004-6361/201220629
23. D. Morate et al., Compositional study of asteroids in the Erigone collisional family using visible spectroscopy at the 10.4 m GTC. *Astrophs. Astron.* **586**, A129 (2016). doi: 10.1051/0004-6361/201527453
24. K. Kitazato et al., Surface composition of asteroid 162173 Ryugu as observed by the Hayabusa2 NIRS3 instrument. *Science*, this issue (2019).
25. J. de León et al., Expected spectral characteristics of (101955) Bennu and (162173) Ryugu, targets of the OSIRIS-REx and Hayabusa2 missions. *Icarus* **313**, 25–37 (2018). doi: 10.1016/j.icarus.2018.05.009
26. T. Hiroi, C. M. Pieters, M. E. Zolenski, M. E. Lipschutz, Thermal metamorphism of the C, G, B, and F asteroids seen from the 0.7-µm, 3-µm, and UV absorption strengths in comparison with carbonaceous chondrites. *Meteorit. Planet. Sci.* **31**, 321–327 (1996). doi: 10.1111/j.1945-5100.1996.tb02068.x
27. E. Tonui et al., Petrographic, chemical and spectroscopic evidence for thermal metamorphism in carbonaceous chondrites I: CI and CM chondrites. *Geochim. Cosmochim. Acta* **126**, 284–306 (2014). doi: 10.1016/j.gca.2013.10.053
28. P. Vernazza et al., Interplanetary dust particles as samples of icy asteroids. *Astrophys. J.* **806**, 204, (2015). doi: 10.1088/0004-637X/806/2/204
29. S. Fornasier, C. Lantz, M. A. Barucci, M. Lazzarin, Aqueous alteration on main belt primitive asteroids: Results from visible spectroscopy. *Icarus* **233**, 163–178 (2014). doi: 10.1016/j.icarus.2014.01.040

30. J. M. Bauer, et al., The NEOWISE-Discovered Comet Population and the CO + CO_2, Production Rates. *Astrophys. J.* **814**, 85 (2015). doi:10.1088/0004-637X/814/2/85
31. B. E. Clark et al., NEAR Photometry of asteroid 253 Mathilde. *Icarus* **140**, 53–65 (1999). doi: 10.1006/icar.1999.6124
32. E. A. Cloutis, P. Hudon, T. Hiroi, M. J. Gaffey, Spectral reflectance properties of carbonaceous chondrites 4: Aqueously altered and thermally metamorphosed meteorites. *Icarus* **220**, 586–617 (2012). doi: 10.1016/j.icarus.2012.05.018
33. T. Nakamura, Post-hydration thermal metamorphism of carbonaceous chondrites. *J. Mineral. Petrolog. Sci.* **100**, 260–272 (2005). doi: 10.2465/jmps.100.260
34. E. A. Cloutis et al., Spectral reflectance properties of carbonaceous chondrites: 1. CI chondrites. *Icarus* **212**, 180–209 (2011). doi: 10.1016/j.icarus.2010.12.009
35. E. A. Cloutis et al., Spectral reflectance properties of carbonaceous chondrites: 2. CM chondrites. *Icarus* **216**, 309–346 (2011). doi: 10.1016/j.icarus.2011.09.009
36. M. Delbo et al., Thermal fatigue as the origin of regolith on small asteroids. *Nature* **508**, 233–236 (2014). doi: 10.1038/nature13153
37. S. Marchi et al., Heating of near-Earth objects and meteoroids due to close approaches to the Sun. *Mon. Not. R. Astron. Soc.* **400**, 147–153 (2009). doi:10.1111/j.1365-2966.2009.15459.x
38. S. C. Koga et al., Spectral decomposition of asteroid Itokawa based on principal component analysis. *Icarus* **299**, 386–395 (2018). doi: 10.1016/j.icarus.2017.08.016
39. T. G. Müller, et al., Hayabusa-2 mission target asteroid 162173 Ryugu (1999 JU3): Searching for the object's spin-axis orientation. *Astron. Astrophys.* **599**, A103 (2017). doi: 10.1051/0004-6361/201629134
40. N. Sakatani et al., Thermal conductivity model for powdered materials under vacuum based on experimental studies. *AIP Adv.* **7**, 015310 (2017). doi: 10.1063/1.4975153
41. E. Cloutis et al., Spectral reflectance "deconstruction" of the Murchison CM2 carbonaceous chondrite and implications for spectroscopic investigations of dark asteroids. *Icarus* **305**, 203–224 (2018). doi: 10.1016/j.icarus.2018.01.015
42. T. Michikami et al., Size-frequency statistics of boulders on global surface of asteroid 25143 Itokawa. *Earth Planet. Space* **60**, 13–20 (2008). doi: 10.1186/BF03352757
43. P. C. Thomas, J. Veverka, M. S. Robinson, S. Murchie, Shoemaker crater as the source of most ejecta blocks on the asteroid 433 Eros. *Nature* **413**, 394–396 (2001). doi: 10.1038/35096513
44. S. Mazrouei, M. G. Daly, O. S. Barnouin, C. M. Ernst, I. DeSouza, Block distribution on Itokawa. *Icarus* **229**, 181–189 (2014). doi: 10.1016/j.icarus.2013.11.010
45. Y. Jiang et al. Boulders on asteroid Toutatis as observed by Chang'e-2. *Sci. Rep.* **5**, 16029 (2015). doi: 10.1038/srep16029
46. H. Demura et al., Pole and Global Shape of 25143 Itokawa. *Science* **312**, 1347–1349 (2006). doi: 10.1126/science.1126574
47. H. Miyamoto et al., Regolith Migration and Sorting on Asteroid Itokawa. *Science* **316**, 1011–1014 (2007). doi: 10.1126/science.1134390
48. J. Veverka et al., Imaging of Small-Scale Features on 433 Eros from NEAR: Evidence for a Complex Regolith. *Science* **292**, 484–488 (2001). doi: 10.1126/science.1058651
49. A. Bischoff, et al., Nature and origins of meteoritic breccias. in Meteorites and the Early Solar System II, University of Arizona Press, Arizona, pp. 679–712 (2006).

50. P. Michel et al., Selective sampling during catastrophic disruption: Mapping the location of reaccumulated fragments in the original parent body. *Planet. Space Sci.* **107**, 24–28 (2015). doi: 10.1016/j.pss.2014.08.005
51. S. Wakita, M. Sekiya, Thermal Evolution of Icy Planetesimals in the Solar Nebula. *Earth Planet. Space* **63**, 1193–1206 (2011). doi: 10.5047/eps.2011.08.012
52. G. D. Cody et al., Organic thermometry for chondritic parent bodies. *Earth Planet. Sci. Lett.* **272**, 446–455 (2008). doi: 10.1016/j.epsl.2008.05.008
53. F. Herbert, C. P. Sonett, M. J. Gaffey, Protoplanetary thermal metamorphism: The hypothesis of electromagnetic induction in the protosolar wind, in The Sun in time. University of Arizona Press, Tucson, pp. 710–739 (1991).
54. W. F. Bottke, M. C. Nolan, R. Greenberg, R. A. Kolvoord, Velocity distributions among colliding asteroids. *Icarus* **107**, 255–268 (1994). doi: 10.1006/icar.1994.1021
55. N. A. Moskovitz et al., Rotational characterization of Hayabusa II target Asteroid (162173) 1999 JU3. *Icarus* **224**, 24–31 (2013). doi: 10.1016/j.icarus.2013.02.009
56. S. J. Bus, R. P. Binzel, Phase II of the small main-belt asteroid spectroscopic survey. A feature-based taxonomy. *Icarus* **158**, 106-145 (2002). doi: 10.1006/icar.2002.6857
57. M. Matsuoka et al., An evaluation method of reflectance spectra to be obtained by Hayabusa2 Near-Infrared Spectrometer (NIRS3) based on laboratory measurements of carbonaceous chondrites. *Earth Planet. Space* **69**, 120 (2017). doi: 10.1186/s40623-017-0705-4
58. C. M. Pieters, Strength of mineral absorption features in the transmitted component of near-infrared reflected light: First results from RELAB. *J. Geophys. Res.* **88**, 9534–9544 (1983). doi: 10.1029/JB088iB11p09534
59. M. Matsuoka et al., Pulse-laser irradiation experiments of Murchison CM2 chondrite for reproducing space weathering on C-type asteroids. *Icarus* **254**, 135–143 (2015). doi: 10.1016/j.icarus.2015.02.029
60. F. Vilas, New spectral reflectance observations of Hayabusa 2 near-Earth asteroid target 162173 1999 JU3. *Amer. Astron. Soc.*, *44th DPS meeting*, Abstract #102.03. (2012).
61. D. Perna et al., Spectral and rotational properties of near-Earth asteroid (162173) Ryugu, target of the Hayabusa2 sample return mission. *Astron. Astrophys.* **599**, L1 (2017). doi: 10.1051/0004-6361/201630346.
62. B. Hapke, Theory of Reflectance and Emittance Spectroscopy. Cambridge University Press, New York, 2nd Edition, p. 513 (2012).
63. D. L. Domingue, S. L. Murchie, N. L. Chabot, B. W. Denevi, F. Vilas, Mercury's spectrophotometric properties: Update from the Mercury Dual Imaging System observations during the third MESSENGER flyby. *Planet. Space Sci.* **59**, 1853–1872 (2011). doi: 10.1016/j.pss.2011.04.012
64. D. L. Domingue et al., Photometric correction of Mercury's global color mosaic. *Planet. Space Sci.* **59**, 1873–1887 (2011). doi: 10.1016/j.pss.2011.04.012
65. D. L. Domingue, S. L. Murchie, B. W. Denevi, C. M. Ernst, N. L. Chabot, Mercury's global color mosaic: An update from MESSENGER's orbital observations, *Icarus* **257**, 477–488 (2015). doi: 10.1016/j.icarus.2014.11.027
66. B. Hapke, Bidirectional reflectance spectroscopy, 1. Theory. *J. Geophys. Res.* **68**, 4571–4586 (1981). doi: 10.1029/JB086iB04p03039
67. T. Fukuhara et al., LIR: longwave infrared camera onboard the Venus orbiter Akatsuki. *Earth Planets Space* **63**, 1009–1018 (2011). doi: 10.5047/eps.2011.06.019

68. T. Okada et al., Earth and Moon Observations by Thermal Infrared Imager on Hayabusa2 and the application to detectability of Asteroid 162173 Ryugu, *Planet. Space Sci.* **158**, 46–52 (2018). doi: 10.1016/j.pss.2018.05.007
69. K. Endo et al., HEAT: Image and database browser for the thermal imager on Hayabusa2, *IEEE Aerospace Conf. Proc.* (2017). doi: 10.1109/AERO.2017.7943827
70. A. F. Cheng et al., Small-scale topography of 433 Eros from laser altimetry and imaging. *Icarus* **155**, 51–74 (2002). doi: 10.1006/icar.2001.6750
71. S. J. Robbins et al., Measuring impact crater depth throughout the solar system. *Meteorit. Planet. Sci.* **43**, 1–44 (2017). doi: 10.1111/maps.12956
72. W. F. Bottke Jr., R. Greenberg, Asteroidal collision probabilities. *Geophys. Res. Lett.* **20**, 879–991 (1993). doi: 10.1029/92GL02713
73. D. P. O'Brien, R. Greenberg, J. E. Richardson, Craters on asteroids: Reconciling diverse impact records with a common impacting population. *Icarus* **183**, 78–92 (2006). doi: 10.1016/j.icarus.2006.02.008
74. H. J. Melosh, Impact Cratering: A Geologic Process. Oxford Univ. Press, New York (1989).
75. K. A. Holsapple, The scaling of impact processes in planetary sciences. *Annu. Rev. Earth Planet. Sci.* **21**, 333–373 (1993). doi: 10.1146/annurev.ea.21.050193.002001
76. K.A. Holsapple, K.R. Housen, A crater and its ejecta: An interpretation of Deep Impact. *Icarus*, **191**, 586–597 (2007). doi:10.1016/j.icarus.2006.08.035
77. G. J. Flynn, Physical properties of meteorites and interplanetary dust particles: clues to the properties of the meteors and their parent bodies. *Earth Moon Planets* **95**, 361–374 (2004). doi:10.1007/s11038-005-9025-y
78. E. F. Tedesco, D. J. Tholen, B. Zellner, The eight-color asteroid survey - Standard stars. *Astron. J.* **87**, 1585–1592 (1982). doi:10.1086/113248
79. C. Lantz, R. P. Binzel, F. E. DeMeo, Space weathering trends on carbonaceous asteroids: A possible explanation for Bennu's blue slope? *Icarus* **302**, 10–17 (2018). doi: 10.1016/j.icarus.2017.11.010
80. D. M. Applin et al., Ultraviolet spectral reflectance of carbonaceous materials. *Icarus* **307**, 40–82 (2018). doi: 10.1016/j.icarus.2018.02.012
81. D. C. Richardson, T. Quinn, J. Stadel, G. Lake, Direct Large-Scale *N*-body Simulations of Planetesimal Dynamics. *Icarus* **143**, 45–49 (2000). doi: 10.1006/icar.1999.6243
82. P. Michel, W. Benz, D. C. Richardson, Disruption of fragmented parent bodies as the origin of asteroid families. *Nature* **421**, 608–611 (2003). doi: 10.1038/nature01364
83. M. Jutzi, P. Michel, D. C. Richardson, Fragment properties from large-scale asteroid collisions: I: Results from SPH/N-body simulations using porous parent bodies and improved material models. *Icarus* **317**, 215–228 (2019). doi: 10.1016/j.icarus.2018.08.006
84. M. Jutzi, W. Benz, P. Michel, Numerical simulations of impacts involving porous bodies: I. Implementing sub-resolution porosity in a 3D SPH hydrocode. *Icarus* **198**, 242–255 (2008). doi: 10.1016/j.icarus.2008.06.013
85. M. Jutzi, P. Michel, K. Hiraoka, A. M., Nakamura, W. Benz, Numerical simulations of impacts involving porous bodies: II. Comparison with laboratory experiments. *Icarus* **201**, 802–813 (2009). doi: 10.1016/j.icarus.2009.01.018
86. M. Jutzi, P. Michel, W. Benz, D. C. Richardson, Fragment properties at the catastrophic disruption threshold: The effect of the parent body's internal structure. *Icarus* **207**, 54–65 (2010). doi: 10.1016/j.icarus.2009.11.016

87. O. Abramov, D. A. Kring, S. J. Mojzsis, The impact environment of the Hadean Earth, *Chemie der Erde* **73**, 227–248 (2013). doi: 10.1016/j.chemer.2013.08.004

Acknowledgments: We thank the anonymous reviewers for their helpful comments. The Hayabusa2 spacecraft was developed and built under the leadership of Japan Aerospace Exploration Agency (JAXA), with contributions from the German Aerospace Center (DLR) and the Centre National d'Études Spatiales (CNES), and in collaboration with NASA, Nagoya Univ., Univ. of Tokyo, National Astronomical Observatory of Japan (NAOJ), Univ. of Aizu, Kobe Univ., and other universities, institutes, and companies in Japan. We also thank many engineers, including Noriyasu Inaba at JAXA and Tetsuya Masuda, Seiji Yasuda, Kouta Matsushima, and Takeshi Ohshima at NEC Corp. for their dedicated work on the Hayabusa2 mission, Koshi Sato at NEC Corp. for ONC development, Shingo Kashima at NAOJ for optical calculations, and Yoshiko Baba at UTOPS for illustrating Fig. 8. **Funding:** This study was supported by KAKENHI from the Japanese Society for Promotion of Science (JSPS) (Grant Nos. JP25120006, 17H01175, JP17H06459, JP17K05639, JP16H04059, JP17KK0097, JP26287108, JP16H04044) and the JSPS Core-to-Core program "International Network of Planetary Sciences." P.M. and M.A.B. acknowledge funding support from the French space agency CNES. P.S. acknowledges funding from Academies of Excellence: Complex systems and Space, environment, risk, and resilience, part of the IDEX JEDI of the Université Côte d'Azur in connection with its Center for Planetary. TM has received funding from the European Union's Horizon 2020 Research and Innovation Programme, under Grant Agreement no 687378. D.D.L, C.M.E., L.L.C., and M.K. acknowledges funding through the NASA Hayabusa2 Participating Scientist Program. **Author contributions:** S.Su. coordinated coauthor contributions, led the ONC data acquisition, analyses, and interpretations, and wrote the paper with contributions from D.D., T.Ok, N.Na, T.M., and R.L.B.. ONC data acquisitions and reductions: R.Ho., T.Mo., I.Y., S.Ka. H.Sa., E.T., C.Ho., Y.Y., M.Ya., T.K., N.Sa., K.Og., H.Su., K.Yoshioka, M.Ha., Y.C., M.M., D.D., H.K.; Geomorphology analyses: H.M., T.Mo., E.T., C.H., T.Mi., Y.C., M.Hi., P.M., O.S.B., C.M.E., L.L.C., S.E.S., R.J., K.Ot., N.Sc., H.K., R.He., G.K., T.Mic., S.Sa, P.A.A.; Spectral analysis: E.T., D.D., R.Ho., Y.Y., T.Mo., C.S., N.T., Y.Su., S.Ha., M.I., S.Tac., M.O., K.Na. M.Z., F.V., M.A.B.; TIR data acquisitions and analyses: T.Ok., T.F., S.Tan., M.T., T.A., H.Se., H.D., Y.Og., T.K., N.Sa., Y.Sh., T.Se., T.G.M., A.Ha.; LIDAR data acquisitions and analyses: N.Na, T.Miz., H.Se., H.N., K.M., N.H. (Kobe), R.Y., Y.I., H.I., H.A., K.Ya., S.A., F.Y., A.Hi., S.Sa, S.O., S.Ts., K.A., S.Ta., M.S., H.M., H.D., J.K., T.Ot.; Shape modeling: N.N. (Kobe), N.H. (Aizu), R.N., E.P., R.G., O.S.B., C.M.E., S.W.; R.L.B. conducted 3D numerical calculations. Interpretation and writing contribution: T.M., E.T., D.D., R.Ho, T.Ok., N.Na., T.N., T.H., P.M., O.S.B., C.M.E., S.E.S., H.Ya, M.Z., S.W., M.F.; Science operations of spacecraft: S.Tan., M.Yo., T.I., M.A., M.Ha., T.Ok., R.N., Y.Sh., N.Sa., M.M., H.Yan., R.T., M.O., F.T., N.O., H.Sa., T.Y., S.Ki., Y.Oh., Y.Takao., H.T., G.O., Y.Mi., K.Yoshikawa, T.T., Y.Takei., A.F., C.Hi., S.N., S.Ho., O.M., T.Sh., S.So, K.Ni., T.S., Y.Ts. **Competing interests:** The authors declare no competing financial interests. Y.Ya. is also affiliated with Tokyo Metropolitan University. **Data and materials availability:** The images, original codes, and input data in the paper are available at the JAXA Data Archives and Transmission System (DARTS) website (http://www.darts.isas.jaxa.jp/pub/hayabusa2/paper/Sugita_2019/). Additional data from the mission will be delivered to the DARTS archive at

https://www.darts.isas.jaxa.jp/planet/project/hayabusa2/, and higher-level data products will be available in the Small Bodies Node of the Planetary Data System https://pds-smallbodies.astro.umd.edu/ one year after departure from the asteroid."

Supplementary Materials:
Materials & Methods
Figs. S1 to S15
Tables S1-S3
References (60-87)

Figures

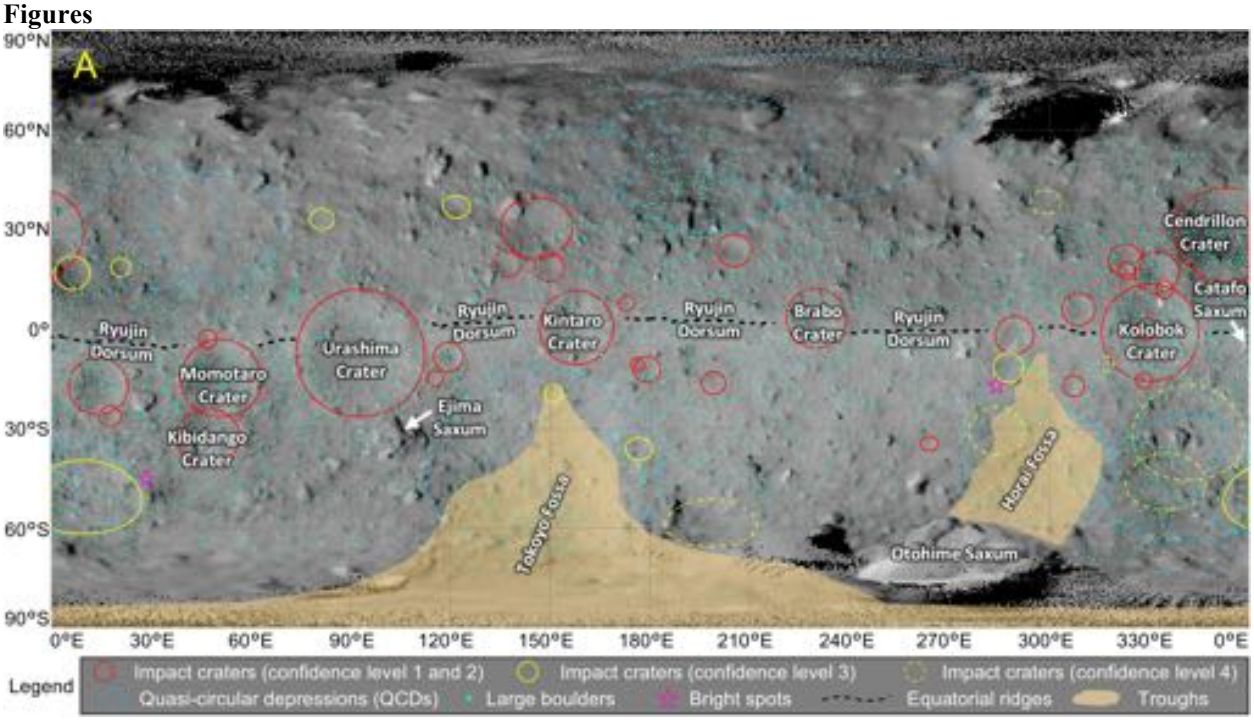

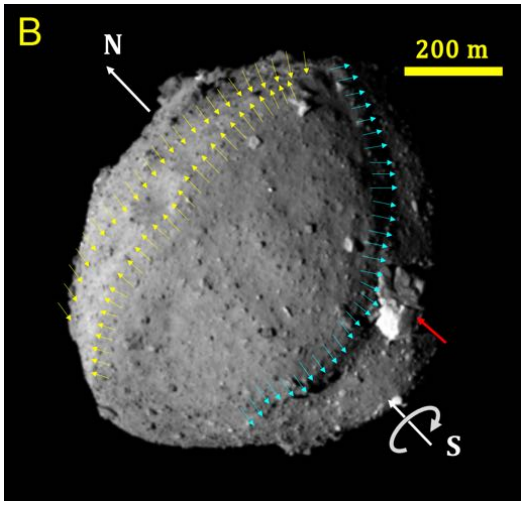

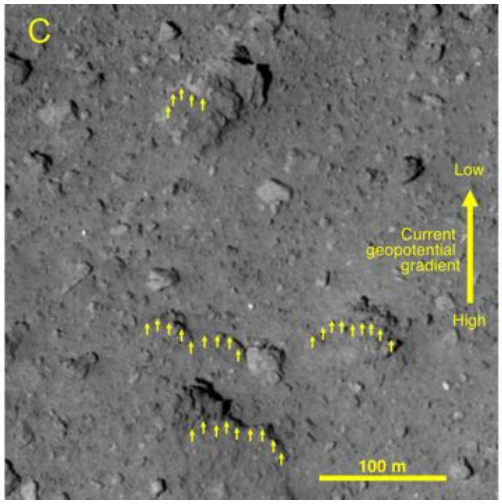

Figure 1. Global map and images of Ryugu. (A) Geologic map of Ryugu based on mosaicked v-band (0.55 μm) images. Impact craters are indicated with circles, color-coded by confidence level. There is greater latitudinal exaggeration of map-projected surface area on Ryugu than for a sphere, because of its diamond-like cross section. This leads to the apparent higher crater number density in the equatorial region of this map. (B) An oblique view of Ryugu (image hyb2_onc_20180824_102748_tvf_l2b), showing the circum-equatorial ridge (yellow arrows), trough (blue arrows) extending from the equatorial region through the south polar region to the other side of Ryugu, and the large and bright Otohime Saxum (red arrow) near the south pole. The location of the poles and the spin direction are indicated with white arrows. (C) Asymmetric regolith deposits on imbricated flat boulders on the northern slope of the circum-equatorial ridge of Ryugu (hyb2_onc_20181003_222509_tvf_l2a). Small yellow arrows at the edges of regolith deposits indicate the direction of mass wasting. The large yellow arrow indicates the current

geopotential gradient from high to low (17). The direction of geopotential gradient is consistent with the mass wasting.

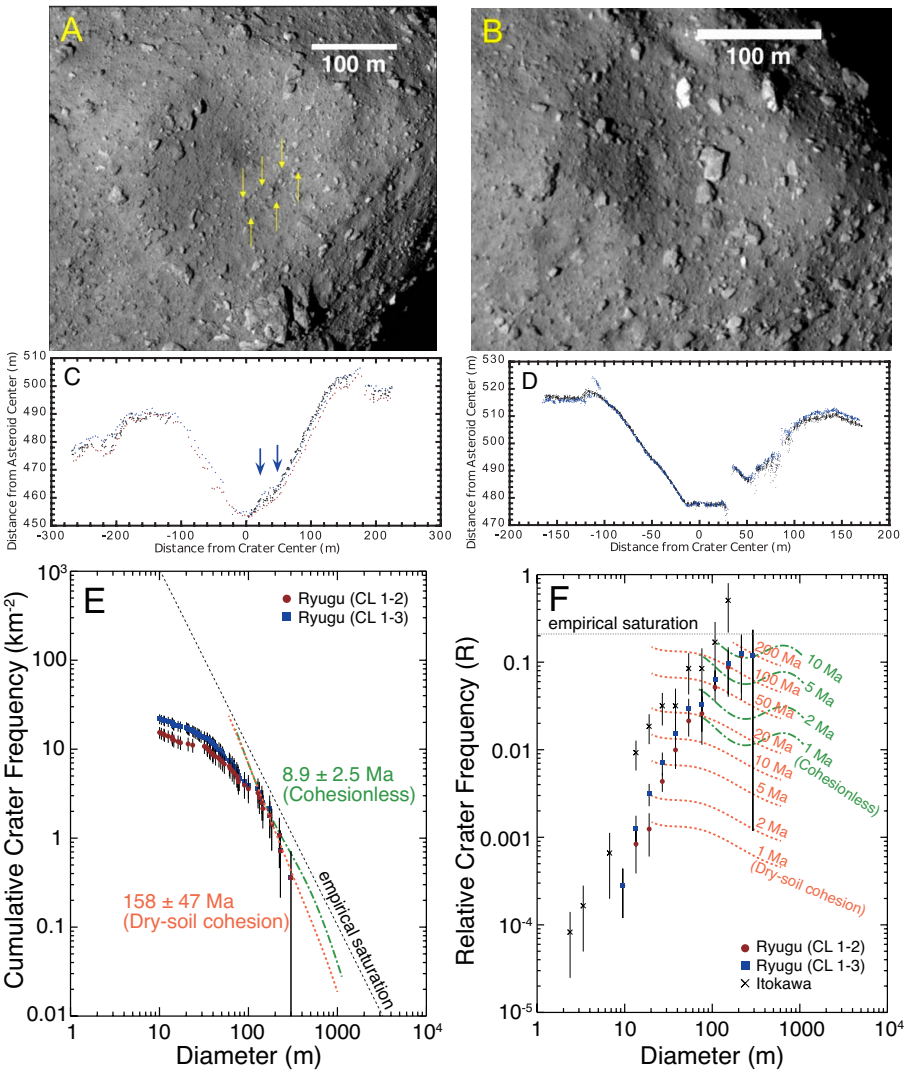

Figure 2. Craters on Ryugu. (A) The largest crater, Urashima (290 m in diameter, 8.3°S, 92.5°E), on Ryugu (hyb2_onc_20180720_071230_tvf_l2b). Wall slumping is indicated with yellow arrows. (B) Kolobok crater (240 m, 1.5°S, 333.5°E), which has a deep floor, bowl-like shape, and a raised rim (hyb2_onc_20180720_100057_tvf_l2b). (C) LIDAR profiles of Urashima crater. Wall slumping is indicated with blue arrows. (D) LIDAR profiles of Kolobok crater. (E) Crater size frequency distribution (CSFD) on Ryugu and Itokawa along with the empirical saturation and crater production curves (54) with (orange) and without (green) dry-soil cohesion. Black crosses are Itokawa crater candidates (11). Red and blue points indicate Ryugu craters are different crater CLs. (F) An R-plot (the CSFD normalized by D^{-2}) for Ryugu (solid symbols) and Itokawa (black crosses). The relative crater frequency R is defined as the differential crater frequency in a diameter range between D/k and kD, divided by D^3, where k is $2^{1/4}$. Saturation and crater production curves are the same as in (E).

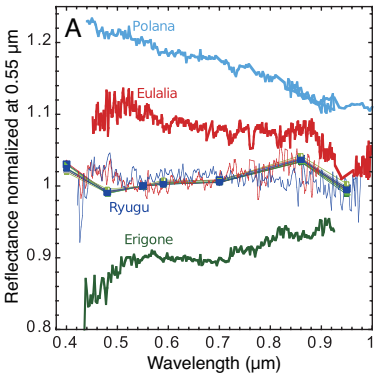
A
Polana
Eulalia
Ryugu
Erigone
Reflectance normalized at 0.55 µm
Wavelength (µm)

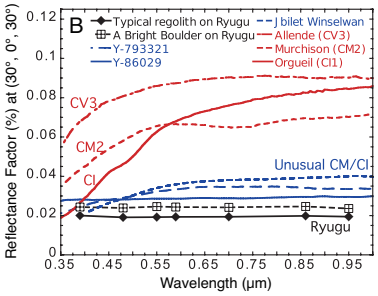
B
Typical regolith on Ryugu
A Bright Boulder on Ryugu
Y-793321
Y-86029
Jbilet Winselwan
Allende (CV3)
Murchison (CM2)
Orgueil (CI1)
CV3
CM2
CI
Unusual CM/CI
Ryugu
Reflectance Factor (%) at (30°, 0°, 30°)
Wavelength (µm)

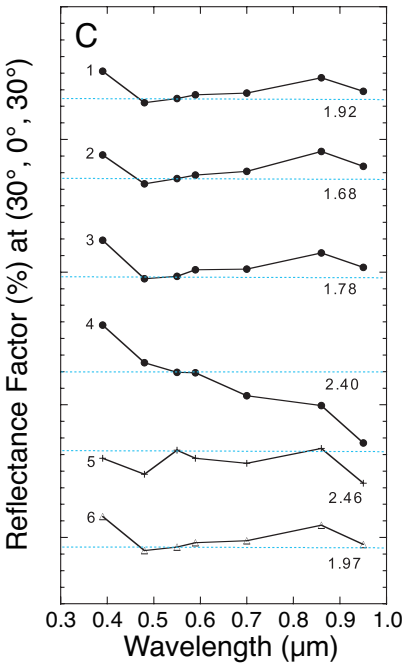
C
1
1.92
2
1.68
3
1.78
4
2.40
5
2.46
6
1.97
Reflectance Factor (%) at (30°, 0°, 30°)
Wavelength (µm)

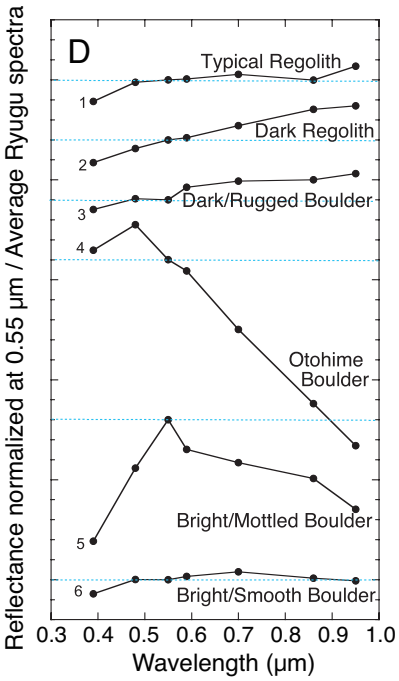
D
Typical Regolith
Dark Regolith
Dark/Rugged Boulder
Otohime Boulder
Bright/Mottled Boulder
Bright/Smooth Boulder
Reflectance normalized at 0.55 µm / Average Ryugu spectra
Wavelength (µm)

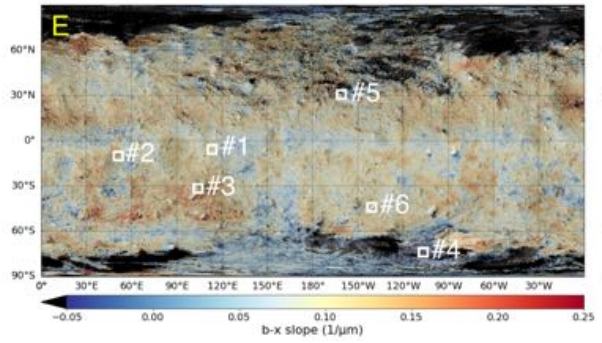
E
#1
#2
#3
#4
#5
#6
b-x slope (1/µm)

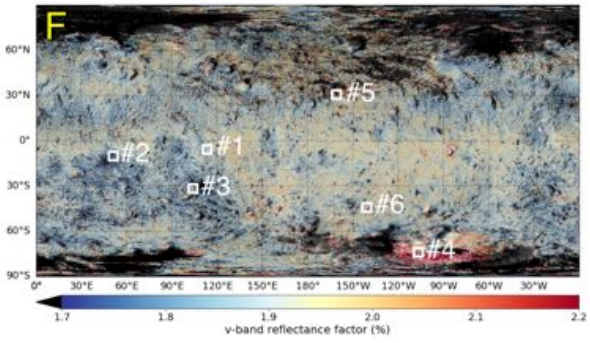
F
#1
#2
#3
#4
#5
#6
v-band reflectance factor (%)

Figure 3. Multi-band colors of Ryugu's surface. (A) A comparison between disk-averaged spectra (lines with squares, normalized at 0.55-μm) for Ryugu at 12 different rotational phases and with ground-based observations (lines without symbols) of Ryugu (55) (blue) and (21) (red), along with the large main-belt asteroids Polana, Eulalia and Erigone (56), each of which is the parent body of an asteroid family. Because of the similarity among the spectra taken at different phases, individual lines for Ryugu overlap. (B) Comparison between typical Ryugu surface colors (black) (reflectance factor at (30°, 0°, 30°)) with those of dehydrated carbonaceous chondrites (blue) and typical carbonaceous chondrites (red). Individual meteorite names are indicated in the figure. The spectrum of powder (≤ 155 μm) sample of Jbilet Winselwan was measured at (30°, 0°, 30°) with the spectrometer system at Tohoku University (57). The rest of meteorite spectra are from (58). (C) The reflectance spectra of typical morphologic/color features on Ryugu, labelled #1 – #6, whose locations are shown in panels (E) and (F) and in Fig. S12. Individual spectra are shifted vertically for clarity. (D) The same as (C) but normalized by the Ryugu average spectrum. (E) b-x slope map (μm^{-1}) and (F) v-band reflectance factor map (%) superposed on a v-band image map. The equatorial ridge and the western side (160°E – 290°E) have slightly higher v-band reflectances than other regions (see Fig. S13 for statistical analysis).

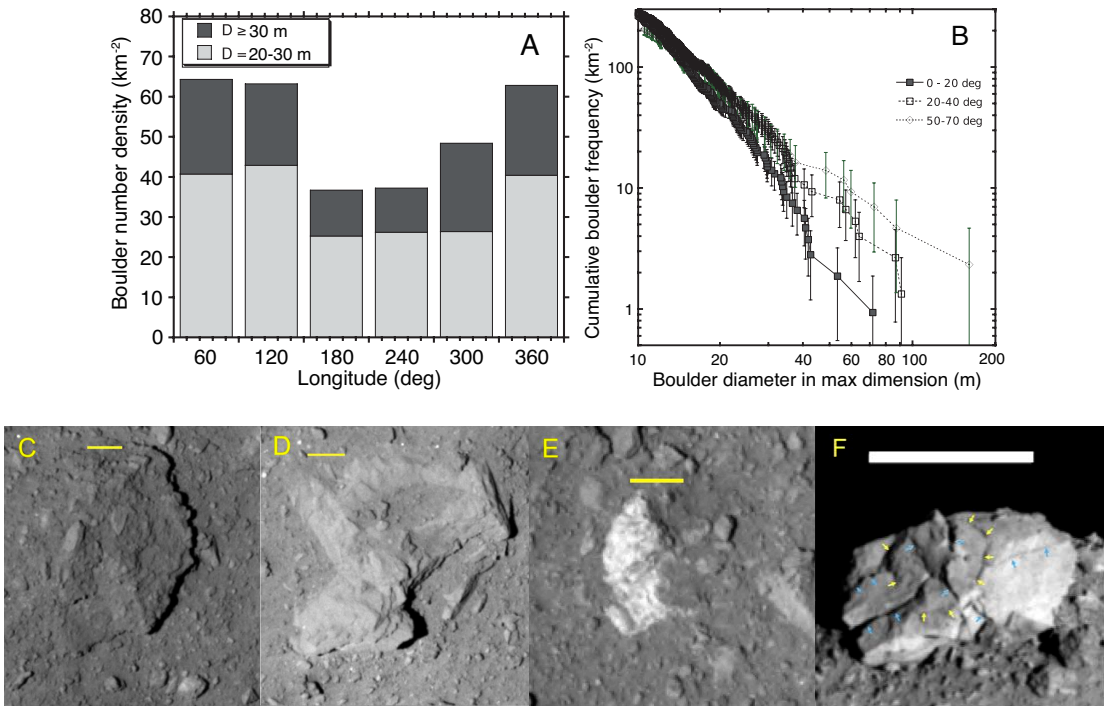

Figure 4. Statistics and morphologies of boulders on Ryugu. The brightness of each image is stretched independently. The yellow and white scale bars are 10 m and 100 m, respectively. (A) Distribution in longitude of boulders with size ranges 20 – 30 m and ≥30 m in diameter. (B) Cumulative size distribution of large boulders, compared among different latitudinal zones. (C) A Type 1 boulder, which is dark and rugged (hyb2_onc_20181004_042509_tvf_l2b). A close up of its layered structure is shown in Fig. S11D. (D) A Type 2 bright boulder with smooth surfaces and thin layered structure (hyb2_onc_20181004_012509_tvf_l2b). A close up of its layered structure is shown in Fig. S11E. (E) A Type 3 bright and mottled boulder (hyb2_onc_20180801_213221_tvf_l2b). (F) The sole Type4 boulder, Otohime Saxum , has concentric (yellow arrows) and radial (blue arrows) fractures, consistent with a fracture system generated by a meteoritic impact (hyb2_onc_20180719_124256_tvf_l2b).

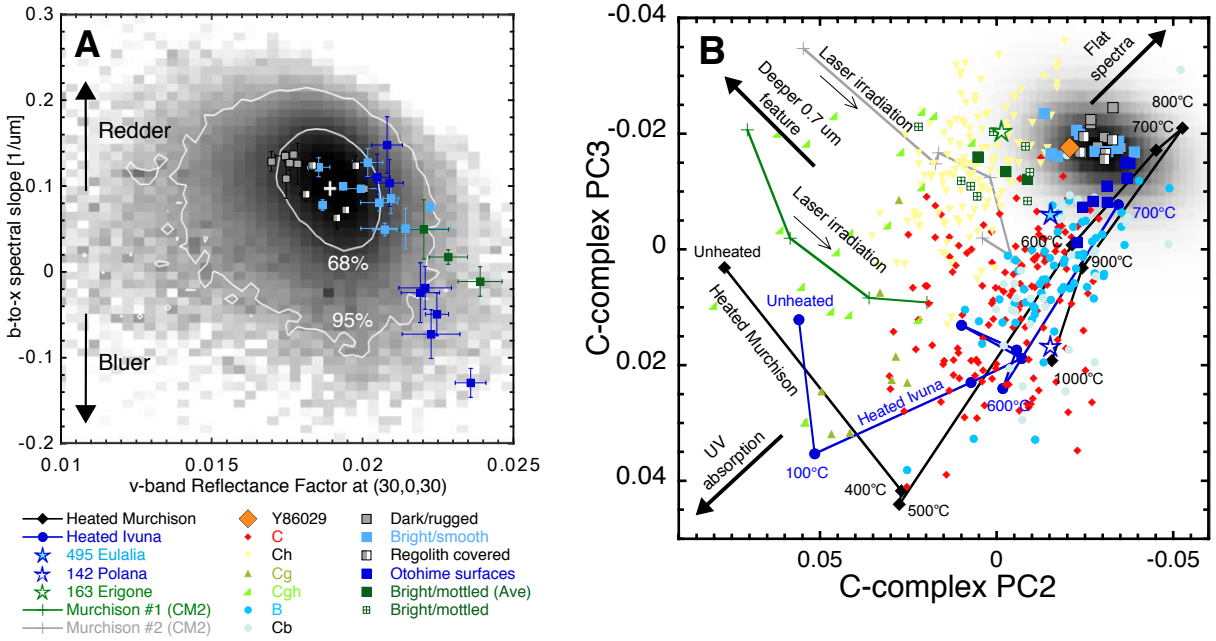

Figure 5. Colors of surface features on Ryugu. Colors measured from ONC-T images are compared between areas of regolith (grey/black contour) and the four types of boulders (solid colored and monotone squares) on Ryugu. The legend applies to both panels. (A) Comparison in v-reflectance factor and b-x slope distribution. The average value of Ryugu's surface is indicated with a white cross. Contours indicate 95% and 68% of the surface area. (B) Comparison in principal-component scores (PC2-PC3) with main-belt C-complex asteroids (56) (colored circles), a moderately dehydrated carbonaceous chondrite (Y 86029, orange diamond (58)), Murchison (CM2) samples with heating (black line (58)) and laser-irradiation (light green (57) and grey lines (58)) experiments, and heated Ivuna (CI) samples (blue line (58)). Parent bodies of major asteroid families in the inner main belt, Polana (blue star), Eulalia (red star), and Erigone (green star), for are also shown (56). Images of the four types of boulders are shown in Figs. 4 and S11. Thick black arrows indicate where end-member spectra are located in this PC space: spectra with deep 0.7-μm absorption, flat spectra, and spectra with deep UV absorption.

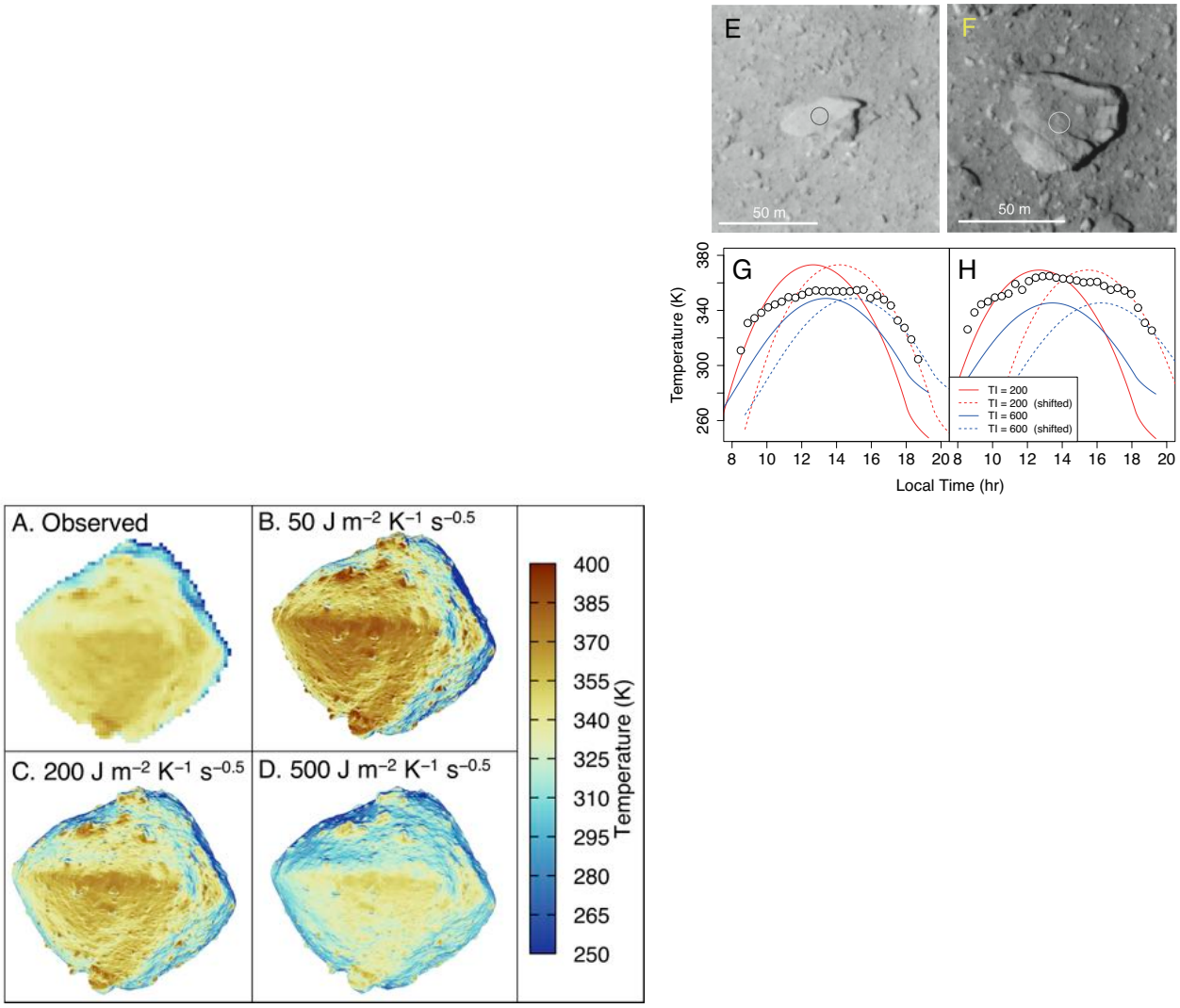

Figure 6. Thermal Infrared camera measurement results. (A) A brightness temperature image taken with TIR at 2018-07-10 06:07:11 (hyb2_tir_20180710_060711_l2). This image is compared with the calculated thermal images using the shape-from-motion (SfM) shape model (17), assuming the uniform thermal inertia of (B) 50, (C) 200, and (D) 500 in J m^{-2} $s^{-0.5}$ K^{-1}, respectively. (E) An ONC-T image of large boulders (6.4°S, 148.4°E) observed during low-altitude observations (5 – 7 km) (hyb2_onc_20180801_144909_tvf_l2b). Surface areas (open circles) not covered with regolith were chosen for temperature analysis. (F) As in (E), but for a boulder at (20.9°S, 27.8°E) (hyb2_onc_20180801_174157_tvf_l2b). (G) The temperature profile of the location indicated with the circle in (E) observed with TIR at 20 km from the Ryugu center (open circles). Theoretical temperature profiles for uniform thermal inertias of 200 and 600 J m^{-2} K^{-1} $s^{-0.5}$ are shown with curves. Solid curves are for a horizonal plane that starts to receive solar light at local time 7.5hr, and dashed curves are for tilted plane enter sunlight at later times. The observed data are largely enclosed by the upper envelopes of time-shifted curves for 200 and 600 J m^{-2} K^{-1} $s^{-0.5}$. (H) Same as (G), but for the location indicated by the circle in (F).

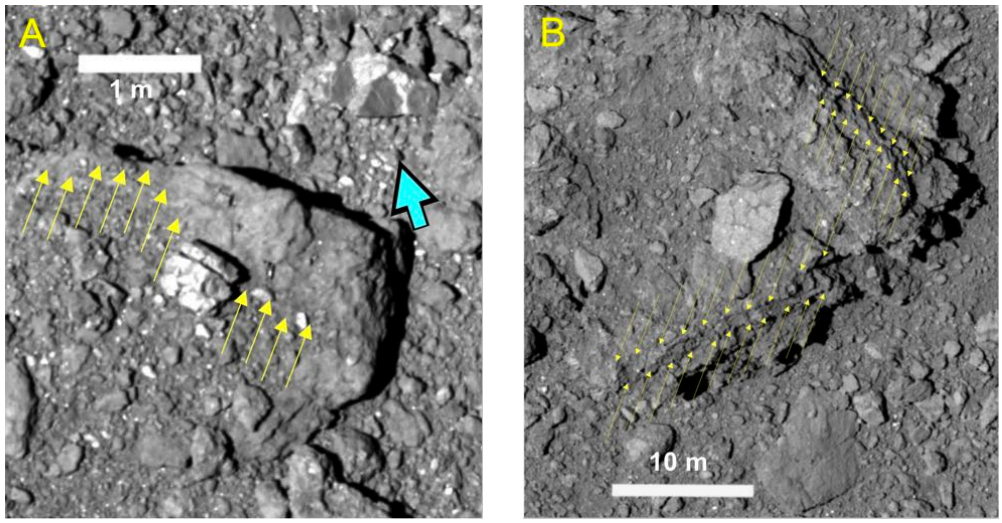

Figure 7. Close-up observation results of surfaces on Ryugu. (A) A boulder partially buried with regolith (small yellow arrows) and a smaller boulder with angular fragments having different brightness (large light blue arrow) near the MINERVA-II landing site (9 mm/pix, hyb2_onc_20180921_040154_tvf_l2b). (B) A rugged boulder with layered structure (small yellow arrows) near the MASCOT landing site (6 cm/pix, hyb2_onc_20181003_003036_tvf_l2b).

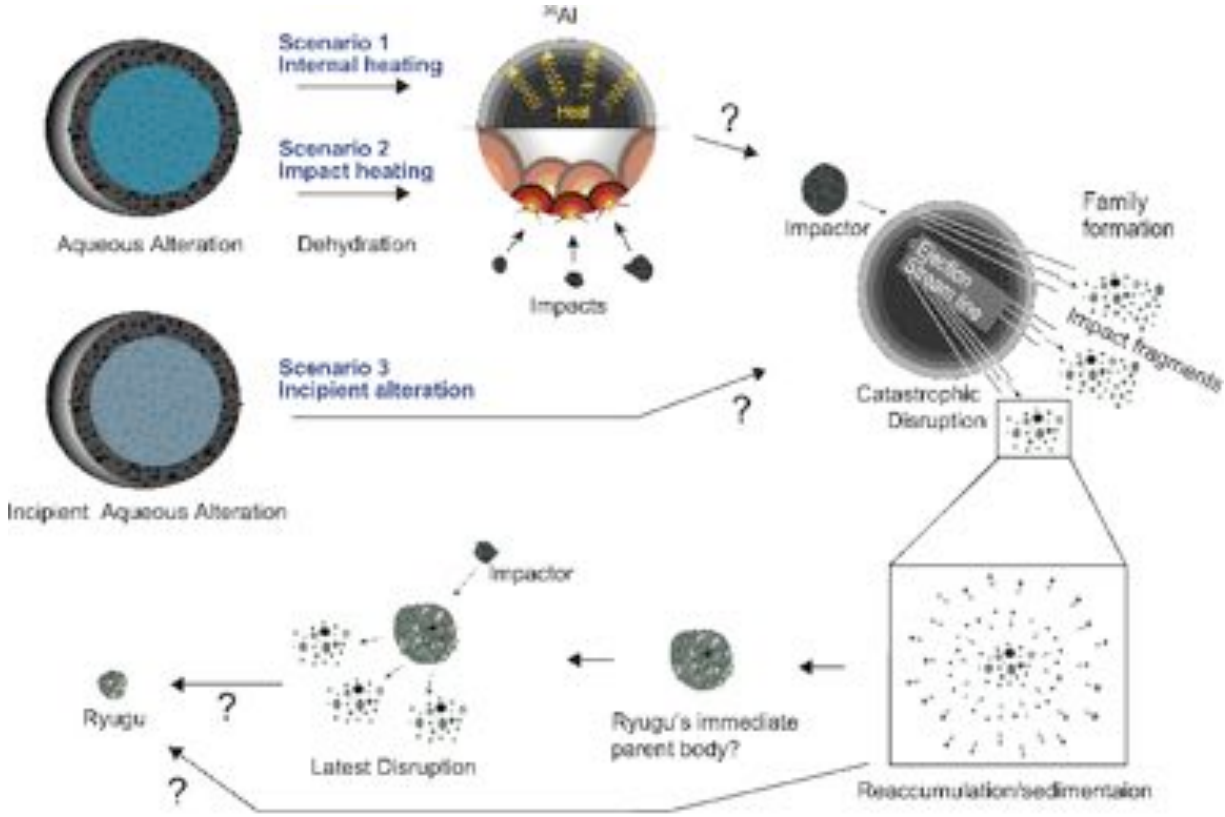

Figure 8. A schematic illustration of Ryugu's formation. Ryugu formed from the re-accumulation of material ejected from an original parent body by an impact, possibly through an intermediate parent body (lower stages). Three scenarios to explain Ryugu's low hydration and

thermal processing may have occurred prior to disruption of the original parent body (upper stages).